

Simulation of Crack Propagation in Asphalt Concrete Using an Intrinsic Cohesive Zone Model

Seong Hyeok Song¹; Glaucio H. Paulino²; and William G. Buttlar³

Abstract: This is a practical paper which consists of investigating fracture behavior in asphalt concrete using an intrinsic cohesive zone model (CZM). The separation and traction response along the cohesive zone ahead of a crack tip is governed by an exponential cohesive law specifically tailored to describe cracking in asphalt pavement materials by means of softening associated with the cohesive law. Finite-element implementation of the CZM is accomplished by means of a user subroutine using the user element capability of the ABAQUS software, which is verified by simulation of the double cantilever beam test and by comparison to closed-form solutions. The cohesive parameters of finite material strength and cohesive fracture energy are calibrated in conjunction with the single-edge notched beam [SE(B)] test. The CZM is then extended to simulate mixed-mode crack propagation in the SE(B) test. Cohesive elements are inserted over an area to allow cracks to propagate in any direction. It is shown that the simulated crack trajectory compares favorably with that of experimental results.

DOI: 10.1061/(ASCE)0733-9399(2006)132:11(1215)

CE Database subject headings: Fractures; Asphalt concrete; Finite element method; Cracking; Simulation.

Introduction

Cracking has occurred in nearly all types of asphalt overlays due to mechanical and environmental loadings. Because cracking causes water penetration, thereby weakening the foundation of the pavement structure and contributing to increased roughness, a number of studies have been conducted to obtain a better understanding of cracking mechanisms and to tackle the cracking problem in asphalt concrete. Majidzadeh et al. (1971) made an early attempt to study crack propagation using fracture testing. Abdulshafi and Majidzadeh (1985) applied the J-integral concept to fatigue and fracture of asphalt mixtures in conjunction with a disk-shaped specimen. Kim and El Hussein (1995) used three-point bending tests to explore fracture behavior of asphalt concrete and to evaluate fracture toughness of asphalt concrete at low temperatures. Jacobs et al. (1996) employed Paris' law to analyze cracking in asphalt concrete and to obtain more insight into the

crack propagation and resistance of asphalt mixes. Bhurke et al. (1997) developed a test protocol to calculate fracture toughness of asphalt concrete at low temperatures. Castell et al. (2000) investigated fatigue crack growth in a laboratory beam specimen and layered pavements using the code Franc2D/L. Several other researchers (Owusu-Antwi et al. 1998; Shen and Kirkner 1999; Sangpetngam et al. 2004) have applied fracture mechanics principles in the study of cracking in asphalt concrete laboratory specimens and pavements. However, most studies of fracture of asphalt concrete have been limited either to experimental investigation or to the analysis of stationary cracks. In this work, a powerful numerical scheme using the cohesive zone model (CZM) concept is introduced to investigate the fracture behavior of asphalt concrete and to simulate crack initiation and propagation of both mode I and mixed-mode cracks.

Cohesive zone models have been used to simulate fracture of both homogeneous and nonhomogeneous materials. Barenblatt (1959, 1962) proposed an early cohesive model to study brittle fracture, and Dugdale (1960) adopted a process zone concept to investigate materials exhibiting plasticity. Xu and Needleman (1994) presented an intrinsic potential-based model where cohesive elements are inserted along either lines or regions in advance, and they implemented this model by means of the finite-element method. Despite great success in simulating crack propagation, this type of cohesive model introduces artificial compliance due to the initial prepeak slope of the intrinsic cohesive law. To alleviate such problems, Espinosa and Zavattieri (2003) used a bilinear model to reduce the compliance by adjusting the initial slope of the cohesive law. An alternative cohesive law was proposed by Camacho and Ortiz (1996). They presented a stress-based extrinsic cohesive law where a new surface is adaptively created by duplicating nodes that were previously bonded. Subsequent investigations were carried out to apply the cohesive fracture modeling in several areas, such as concrete (Mosalam and Paulino 1997; Ruiz et al. 2001), dynamic crack growth (Siegmund and Needleman 1997; Ruiz et al. 2001), viscoelasticity (Rahulkumar et al.

¹Graduate Research Assistant, Dept. of Civil and Environmental Engineering, Univ. of Illinois at Urbana-Champaign, 2204 Newmark Laboratory, 205 North Mathews Ave., MC-250, Urbana, IL 61801. E-mail: shsong@uiuc.edu

²Professor, Dept. of Civil and Environmental Engineering, Univ. of Illinois at Urbana-Champaign, 2209 Newmark Laboratory, 205 North Mathews Ave., MC-250, Urbana, IL 61801 (corresponding author). E-mail: paulino@uiuc.edu

³Associate Professor, Dept. of Civil and Environmental Engineering, Univ. of Illinois at Urbana-Champaign, 1212 Newmark Laboratory, 205 North Mathews Ave., MC-250, Urbana, IL 61801. E-mail: buttlar@uiuc.edu

Note. Associate Editor: Arif Masud. Discussion open until April 1, 2007. Separate discussions must be submitted for individual papers. To extend the closing date by one month, a written request must be filed with the ASCE Managing Editor. The manuscript for this paper was submitted for review and possible publication on March 29, 2005; approved on December 20, 2005. This paper is part of the *Journal of Engineering Mechanics*, Vol. 132, No. 11, November 1, 2006. ©ASCE, ISSN 0733-9399/2006/11-1215-1223/\$25.00.

2000), nonhomogeneous materials, and plasticity (Paulino et al. 2003; Jin et al. 2003).

For pavements, Soares et al. (2003) applied a cohesive zone model in order to investigate crack propagation of the Superpave indirect tension test (IDT) using the cohesive law proposed by Tvergaard (1990). Paulino et al. (2004) proposed an intrinsic cohesive model for asphalt concrete, which is based on the energy potential approach of Xu and Needleman (1994). They determined material strength and cohesive fracture energy with the IDT and single-edge notch beam [SE(B)] test, respectively. Crack propagation in the IDT was simulated with the cohesive parameters calibrated from the SE(B) test using a user-defined subroutine (UEL) in ABAQUS. Recently, Song et al. (2005) explored a bilinear CZM to reduce a compliance. However, most crack propagation simulations conducted thus far using the CZM (Soares et al. 2003; Paulino et al. 2004) have been limited to IDT test and pure mode I problems. Therefore, the present study addresses the following important aspects of cohesive zone modeling of asphalt concrete: (1) calibration of cohesive parameters, selection of cohesive element sizes, and sensitivity of the results to cohesive parameters; (2) simulation of mixed-mode crack propagation in conjunction with the SE(B) test, in which cohesive elements are inserted over an area to allow cracks to propagate in any direction; (3) comparison of the complete crack trajectory of the present numerical simulation using the Riks method (Crisfield 1980) and the user element (UEL) of ABAQUS (ABAQUS 2002) with that of experimental results.

The remainder of this paper is organized as follows. The second section describes the concept of the cohesive zone model (CZM) and its derivation. The third section illustrates procedures to determine material and cohesive properties. Section 4 provides verification of the CZM that was developed and implemented as a user element (UEL) within ABAQUS. Sections 5 and 6 discuss computational results of crack propagation in pure mode I and mixed-mode SE(B) tests. Section 7 presents the summary and conclusions of the study.

Cohesive Zone Model

The CZM concept is provided herein, and its formulation using the principle of virtual work is presented. The force vector and tangent matrix, which are variables to be defined in the UEL, are formulated. Finally, the potential-based effective CZM is introduced.

CZM Concept

The cohesive zone model provides a computationally efficient way to simulate damage occurring in a process zone located ahead of a crack tip (see Fig. 1). This approach, which involves nonlinear constitutive laws described by the displacement jump and the corresponding traction along the interfaces, provides a phenomenological model to simulate fracture behavior such as crack nucleation, initiation, and propagation.

Fig. 1 illustrates the CZM concept in the opening mode (pure mode I) where T_n and δ_n denote normal traction and normal displacement jump, respectively. The material crack tip indicates a point where traction is zero and the cohesive zone tip is a point where the traction reaches a maximum. The cohesive zone is defined as the region between the material crack tip and the cohesive zone tip where complicated fracture behaviors, including inelasticity, occur. The cohesive surfaces are joined together by a

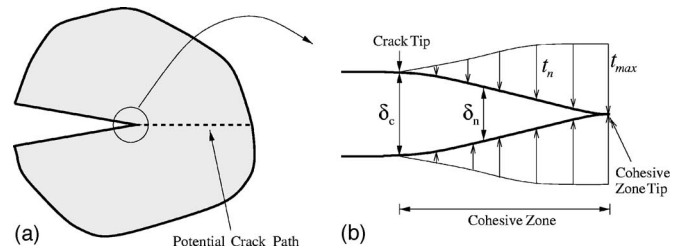


Fig. 1. Schematic representation of: (a) cohesive zone concept; (b) displacement jump (δ_n) and corresponding traction (t_n) along a cohesive surface

cohesive traction, which depends upon the displacement jump across crack faces. As the displacement jump increases due to an increase in external force or compliance in a structure, the traction first increases, then reaches a maximum, and finally decays monotonically to zero. The separation-material response depends on the material strength, critical displacement, and cohesive fracture energy, which represent the cohesive parameters.

CZM Formulation

The principle of virtual work considering the cohesive element contribution is given as

$$\int_V \boldsymbol{\sigma} : \mathbf{D}^* dV - \int_S \mathbf{T} \cdot \boldsymbol{\delta}^* dS - \int_S \mathbf{T} \cdot \mathbf{u}^* dS = 0 \quad (1)$$

where $\boldsymbol{\sigma}$ =Cauchy stress tensor; \mathbf{D}^* =virtual strain tensor; $\boldsymbol{\sigma} : \mathbf{D}^*$ indicates $\sigma_{ij} D_{ji}^*$; \mathbf{T} =traction on the boundary; $\boldsymbol{\delta}^*$ =virtual displacement jump across the cohesive surface; \mathbf{u}^* =virtual displacement in the bulk (background) material; and S and V =current (deformed) surface and volume, respectively.

An implicit displacement-based finite-element scheme requires evaluation of several terms, such as a force vector and a tangent matrix based on different numerical schemes. Evaluation of the tangent matrix and the force vector is necessary for the iteration of the Newton-Raphson method and the Riks method, and an additional term, which is an incremental load vector, needs to be defined for the iteration of the Riks method (ABAQUS 2002). The force vector and the tangent matrix of the cohesive elements are obtained from the second term of Eq. (1) and the first variation of the second term in Eq. (1), respectively. Notice that the incremental load vector of the cohesive elements to be defined for the Riks method is zero for the CZM, because a cohesive force is an internal force and, as a result, is independent of the Riks load parameter.

The virtual cohesive element work is given as

$$W_{\text{coh}}^* = \int_S (T_n \delta_n^* + T_s \delta_s^*) dS \quad (2)$$

where subscript “coh” indicates cohesive; and T_n and T_s =normal and shear tractions, respectively. Moreover, δ_n^* and δ_s^* are virtual normal and shear displacement, respectively, and can be expressed in terms of the shape functions and virtual nodal displacement jump along the normal and shear direction given by

$$\delta_n^* = \mathbf{N} \bar{\delta}_n^*, \quad \delta_s^* = \mathbf{N} \bar{\delta}_s^* \quad (3)$$

where \mathbf{N} =shape functions relating quantities at nodal points to those at Gauss points; and $\bar{\delta}_n^*$ and $\bar{\delta}_s^*$ =virtual normal and shear

displacement jump at the nodal points, respectively.

Substituting Eq. (3) into Eq. (2), one obtains

$$W_{\text{coh}}^* = \int_S (T_n \mathbf{N} \bar{\delta}_n^* + T_s \mathbf{N} \bar{\delta}_s^*) dS \quad (4)$$

Thus, the contribution of the force vector due to cohesive elements can be obtained as follows:

$$F_{\text{coh}} = \int_S (T_n \mathbf{N} + T_s \mathbf{N}) dS \quad (5)$$

Notice that Eqs. (4) and (5) are formulated based on the updated Lagrangian formulation.

The first variation of the virtual work, dW_{coh}^* , is obtained from differentiation of Eq. (4) with respect to the displacement jump and is given as

$$dW_{\text{coh}}^* = \int_S (dT_n \mathbf{N} \bar{\delta}_n^* + dT_s \mathbf{N} \bar{\delta}_s^*) dS \quad (6)$$

Notice that T =function of displacement such that dT_n and dT_s cannot be zero.

The relationship between traction and displacement jump is given by the cohesive material Jacobian $[C]$, which is obtained as

$$\begin{Bmatrix} dT_n \\ dT_s \end{Bmatrix} = [C] \begin{Bmatrix} d\delta_n \\ d\delta_s \end{Bmatrix} \quad (7)$$

where $[C]$ is given by

$$[C] = \begin{bmatrix} \partial T_n / \partial \delta_n & \partial T_n / \partial \delta_s \\ \partial T_s / \partial \delta_n & \partial T_s / \partial \delta_s \end{bmatrix}$$

Thus, the tangent matrix is given by the usual expression

$$[K] = \int_S [B]^T [C] [B] dS \quad (8)$$

where $[B]$ =matrix of shape function relating quantities at nodal points to those at Gauss points.

Potential-Based Effective Model

An exponential form for the free energy potential proposed by Xu and Needleman (1994) between the displacement jump and the corresponding traction provides a computationally convenient description of the decohesion process represented by the shape of the constitutive model, the material strength, and the cohesive fracture energy.

The cohesive law for the interface elements (Ortiz and Pandolfi 1999; Roy and Dodds 2001) can be summarized as follows:

$$\mathbf{t} = \frac{\partial \phi}{\partial \delta_n}(\delta_n, \delta_s, \mathbf{q}) \mathbf{n} + \frac{\partial \phi}{\partial \delta_s}(\delta_n, \delta_s, \mathbf{q}) \frac{\delta_s}{\delta_s} \quad (9)$$

where the subscripts n and s =normal and tangential directions; \mathbf{t} =traction; ϕ =free energy potential; δ_n =normal displacement jump; δ_s =shear sliding; \mathbf{n} =unit normal of the interface elements; and \mathbf{q} =vector of internal variables.

The effective displacement and corresponding effective traction for two-dimensional (2D) analysis become:

$$\delta = \sqrt{\delta_n^2 + \beta^2 \delta_s^2}, \quad t = \sqrt{t_n^2 + \beta^{-2} t_s^2} \quad (10)$$

The parameter β , which is defined as the ratio between the maximum normal traction and the shear traction, is introduced to ex-

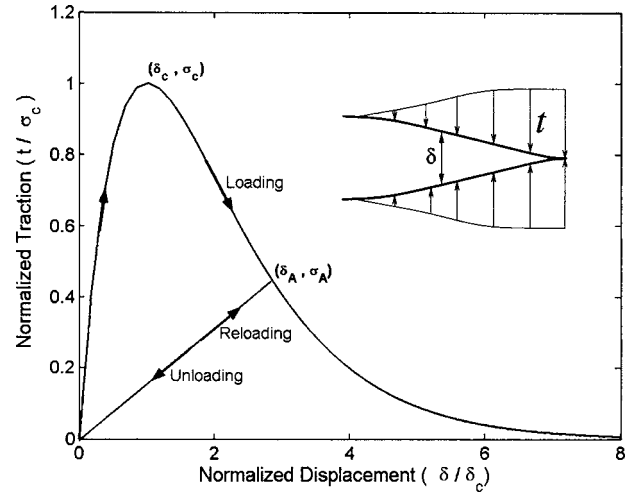


Fig. 2. Schematic representation of loading and unloading in terms of displacement-jump and traction

press the formulation with single effective displacement by assigning different weights for displacements and tractions along the normal and shear directions. In this simulation, $\beta = \sqrt{2}$ (Camacho and Ortiz 1996).

The exponential form for the free energy potential is given (Xu and Needleman 1994) by

$$\phi = e \sigma_c \delta_c \left[1 - \left(1 + \frac{\delta}{\delta_c} \right) \exp\left(-\frac{\delta}{\delta_c} \right) \right] \quad (11)$$

where $e = \exp(1)$; σ_c =material tensile strength; and δ_c =critical displacement. As illustrated in Fig. 2, the relationship between the traction and displacement jump, upon loading, follows the form:

$$t = \frac{\partial \phi}{\partial \delta} = e \sigma_c \frac{\delta}{\delta_c} \exp\left(-\frac{\delta}{\delta_c} \right) \quad (12)$$

and for unloading and reloading, the traction can be obtained with the following expression:

$$t = \left(\frac{t_A}{\delta_A} \right) \quad (13)$$

where subscript A indicates a point where unloading starts to occur in the cohesive law (see Fig. 2). The unloading path follows toward the origin of the cohesive law. The cohesive fracture energy is defined by

$$G_c = \int_0^{\infty} t d\delta = e \sigma_c \delta_c \quad (14)$$

Determination of Bulk and Cohesive Properties

The complex (dynamic) modulus is often used to characterize the time-temperature modulus of asphalt concrete and is used as a material property for the design of asphalt pavement layers (NCHRP 1-37a). In fact, the complex modulus test procedures are currently under review to replace an older version, the ASTM D3497 Test Standard. The essence of the test is to apply a sinusoidal compressive loading on the specimen and to measure the strain response. The complex modulus is simply the amplitude of the stress wave divided by the amplitude of the strain wave. In

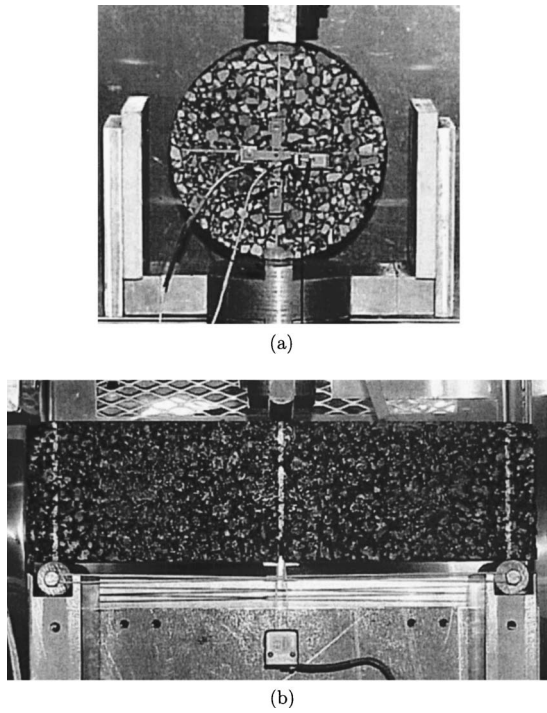


Fig. 3. Experimental setting of: (a) IDT test; (b) SE(B) test

order to capture the time-temperature dependency, the complex modulus is measured over a range of frequencies (25, 10, 5, 1, 0.5, and 0.1 Hz) and temperatures (-10 to 60°C). In this simulation, the Young's modulus is taken as 14.2 GPa based upon complex modulus testing of the mixture at 10°C and 1 Hz.

Two experimental fracture properties of material strength and cohesive fracture energy are evaluated as material inputs into the CZM. The tensile strength of the asphalt concrete is currently determined at -10°C . The first-failure tensile strength determined from the IDT test is defined as the material strength. The procedure for determining the first-failure tensile strength is outlined in the AASHTO TP-9 specification (AASHTO 1996). A material strength of 3.56 MPa was experimentally determined from the IDT test. Fig. 3(a) illustrates the IDT test setting.

The cohesive fracture energy of the asphalt concrete is the other fracture property required as an input into the CZM. The single-edge notched beam [SE(B)] test was used for determining the cohesive fracture energy. The crack-mouth opening displacement (CMOD) was increased at a linear rate to produce a stable postpeak fracture. The CMOD rate was determined by trial and error to produce a peak load at approximately 5 s into the test. Five seconds was selected as the time to peak load based on the AASHTO (1996) TP-9 procedure for determining the tensile strength. The cohesive fracture energy was determined by calculating the area under the load-CMOD curve and normalizing by the cross-sectional area of the beam. At -10°C , a value of 344 J/m^2 was obtained. A detailed procedure for specimen preparation and test controls of the SE(B) test is outlined by Wagoner et al. (2005). Fig. 3(b) shows the SE(B) test apparatus. Notice that both cohesive parameters, evaluated at -10°C , are employed in this study to investigate cracking mechanism occurring under freezing temperatures. For this temperature range, volumetric-cohesive viscoelastic effects are not directly considered.

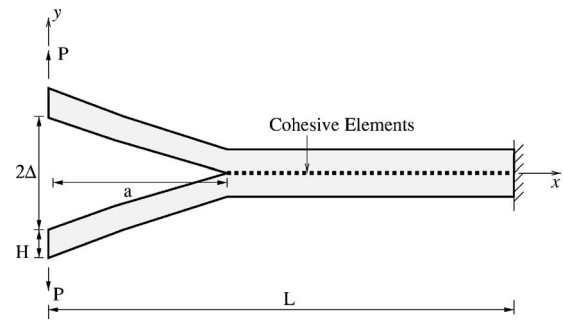


Fig. 4. Schematic drawing of double cantilever beam (DCB) test in which H =thickness; 2Δ =crack mouth opening displacement; L =total length; and a =distance from crack mouth to assumed crack tip location

Verification of CZM

In order to verify the numerical implementation of the aforementioned CZM (i.e., the potential-based exponential model) into the UEL of ABAQUS, a double cantilever beam (DCB) is adopted, because the DCB is well accepted by the fracture community and an analytical solution exists. Using linear elastic beam theory, the analytical solution for crack length in terms of the Young's modulus (E), the end displacement (Δ), the beam height (H), and the cohesive fracture energy (G_c) is obtained (Anderson 1995) as

$$a = \sqrt[4]{\frac{3EH^3\Delta^2}{4G_c}} \quad (15)$$

Fig. 4 illustrates a schematic of the DCB geometry. To avoid shear effects in the beam, a relatively slender DCB of length $L=200\text{ mm}$ and width $H=10\text{ mm}$ is adopted. External displacement is applied to the node located at $x=0$ and $y=0$ upward and downward. Cohesive elements are inserted along the middle of the specimen. Two-dimensional plane strain elements and linear four-node cohesive elements are employed for the bulk material and cohesive material, respectively. To obtain material and cohesive parameters, a 9.5 mm nominal maximum-sized aggregate surface mixture is selected, which is used at the Greater Peoria Regional Airport. The Young's modulus is taken as 14.2 GPa, based upon the aforementioned modulus tests. A Poisson's ratio value of 0.35 is assumed, based upon previous experience with similar materials. The cohesive fracture energy and material strength for this mixture are 344 J/m^2 and 3.56 MPa, respectively. For the exponential model, $0.1\delta_c$ is defined as the crack tip location.

Fig. 5 illustrates a comparison between the numerical and analytical solutions. The abscissa indicates normalized crack length, a/L , and the ordinate indicates the normalized crack opening displacement, δ/δ_c . The numerical results show excellent agreement with the analytical solution. Notice that, even for both the initial stage and final stage of crack propagation, which are influenced by boundary conditions, both numerical and analytical results agree reasonably well.

Mode I Single-Edge Notched Beam [SE(B)] Test

In this section, utilizing the mode I SE(B) test, various important aspects of CZM are presented. First, sensitivity analysis to cohesive parameters of the material strength and cohesive fracture

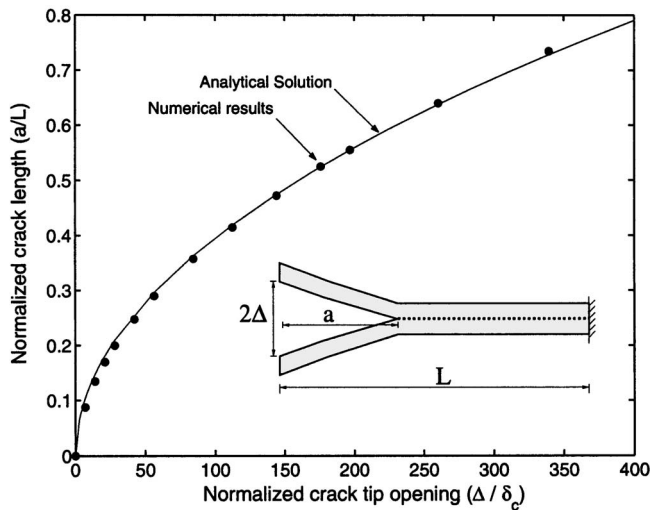


Fig. 5. Comparison between numerical and analytical solutions for DCB specimen

energy is performed. Second, cohesive parameters of material strength and cohesive fracture energy are calibrated by comparing the numerical result with experimental results of the SE(B) test. Finally, justification of the cohesive element size is provided. Three different cohesive element sizes are chosen, and numerical results for each cohesive element size are compared to make sure that the element sizes chosen in the simulation are small enough to capture the nonlinear behavior occurring along the cohesive zone (Klein et al. 2001).

Sensitivity Analysis with Respect to Fracture Energy and Material Strength

Using the condition of small-scale yielding, Tvergaard and Hutchinson (1992) demonstrated that, in general, the influence of the shape of the traction separation law on the numerical responses is relatively weak as compared to other cohesive parameters, e.g., material strength (σ_c) and cohesive fracture energy (G_c). Thus, in this section, the sensitivity analysis to cohesive parameters of material strength and fracture energy is carried out to explore the influence of cohesive parameters, i.e., $\sigma_c = 3.56$ MPa and $G_c = 344$ J/m² (Wagoner et al. 2005).

Fig. 6(a) illustrates a simply supported SE(B) with a length of 376 mm, height of 100 mm, and thickness of 75 mm. A mechanical notch is simulated, which extends 19 mm upward from the bottom edge of the beam. Displacement boundary conditions are imposed at the center of the top edge of the model. Figs. 6(b) and (c) show a finite-element configuration for the whole geometry and the center region of the specimen where the cohesive elements are inserted, respectively. Two-dimensional, four-noded cohesive elements are inserted along the center of the specimen. The bulk material is modeled as elastic, homogeneous, isotropic, and rate independent. These assumptions will be verified in a subsequent study. Given the low test temperature and short test duration, it is assumed that the bulk material can be adequately simulated with elastic materials. In this analysis, $E = 14.2$ GPa and $\nu = 0.35$. The Newton-Raphson method and plane strain conditions are adopted.

Fig. 7(a) illustrates the sensitivity of the P versus CMOD curve to different fracture energies. Three different fracture energies, i.e., $1.2G_c$, G_c , and $0.8G_c$, are employed with a constant value of critical strength. As the fracture energy is increased, the

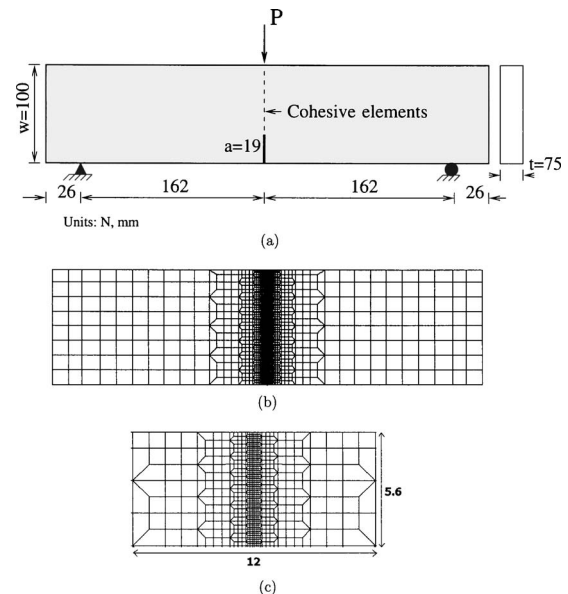


Fig. 6. Geometry and mesh for analysis of SE(B) test: (a) geometry and boundary condition; (b) mesh configuration for whole geometry; and (c) mesh detail along middle of specimen (cohesive elements are inserted along middle line of specimen)

area of the P versus CMOD curve is increased and the maximum load is increased as well. This result is intuitive because, as the intrinsic fracture energy used in the CZM is increased, more global fracture energy is released, which is indicated by an increased area under the P versus CMOD curve. The softening trend, however, seems insensitive to the magnitude of fracture energy. Fig. 7(b) shows the sensitivity of the P versus CMOD curve to different critical strengths, $1.2\sigma_c$, σ_c , and $0.8\sigma_c$. As the critical strength is increased, the maximum load is increased, while the area of the curve remains almost constant.

Calibration of Cohesive Parameters

In the nonlinear cohesive constitutive model, cohesive fracture energy and material strength are two important parameters. These parameters are measured directly from the experiments and reflect the actual viscoelastic heterogeneous material. However, quasi-static homogeneous materials are assumed in the numerical modeling. Thus, the parameters of the CZM model are calibrated by fitting the present numerical results into experimental results in order to take into account these differences between the actual and numerical models.

A first-order calibration of material strength and cohesive fracture energy was accomplished by matching the present numerical results with experimental SE(B) test results (see Fig. 8). Relatively small calibration shifts of the cohesive parameters, i.e., $0.7G_c = 0.7 \times 344$ J/m² and $1.1\sigma_c = 1.1 \times 3.56$ MPa, are required to bring the simulated results into reasonable comparison with the measured results. Notice that, for the rest of simulation, the calibrated cohesive parameters are employed.

Selection of Intrinsic Cohesive Element Size

When the concept of the cohesive zone model is combined with the discrete finite-element method, a numerical issue as to the sensitivity of the size of the cohesive element to the numerical solution arises. This is due to the fact that the cohesive zone is

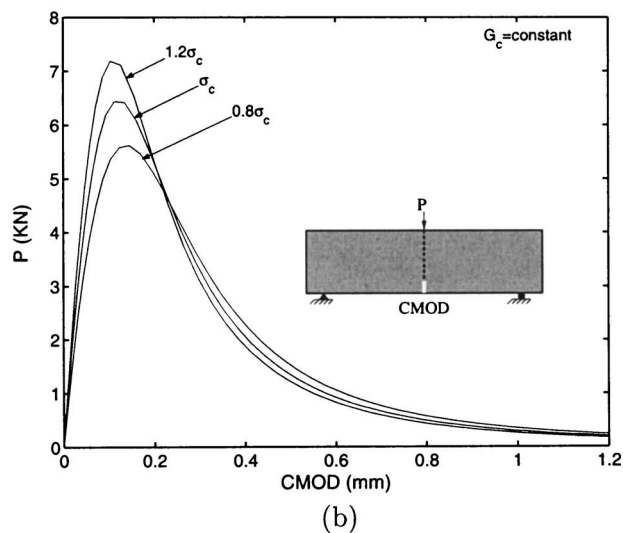
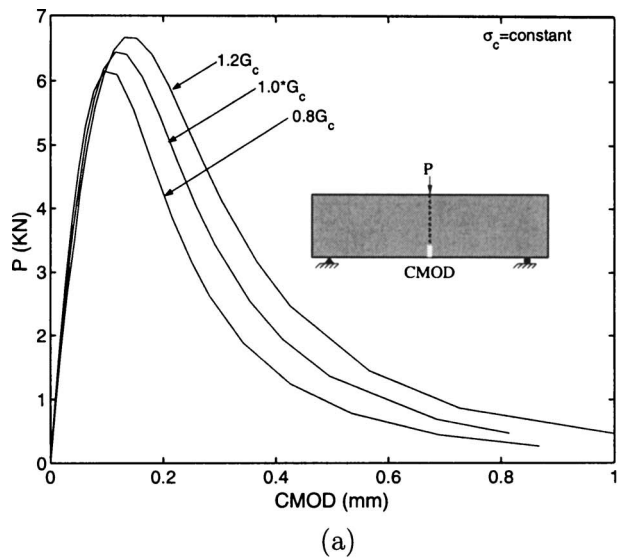


Fig. 7. Sensitivity of P versus CMOD curve to: (a) different fracture energy; (b) different material strength ($\sigma_c = 3.56$ MPa and $G_c = 344$ J/m²)

represented by a highly nonlinear relation between the traction and displacement jump such that enough cohesive elements need to be inserted along the cohesive zone in order to capture the nonlinear softening curve of CZM properly. Camacho and Ortiz (1994) showed that, as the cohesive element size increases, considerable accuracy is lost under dynamic loading. Furthermore, they reported that some of the fragmentation and branching is suppressed when the coarse mesh is adopted. Recently, Klein et al. (2001) explored the influence of cohesive element sizes in conjunction with the double cantilever beam and illustrated that coarse meshes yield accelerated crack growth, i.e., a larger discrepancy between the numerical and analytical solutions. Ruiz et al. (2001) studied mesh size sensitivity to computational results, e.g., reaction versus time curve, simulating SE(B) tests with and without prenotch under dynamic loading. They observed that, for the cracked SE(B), the reaction histories and energy consumption are almost identical for different cohesive element sizes, while for the uncracked SE(B), the cohesive energy consumption is larger for the finer mesh and, as time increases, the discrepancy of the reaction increases for different cohesive element sizes. A general

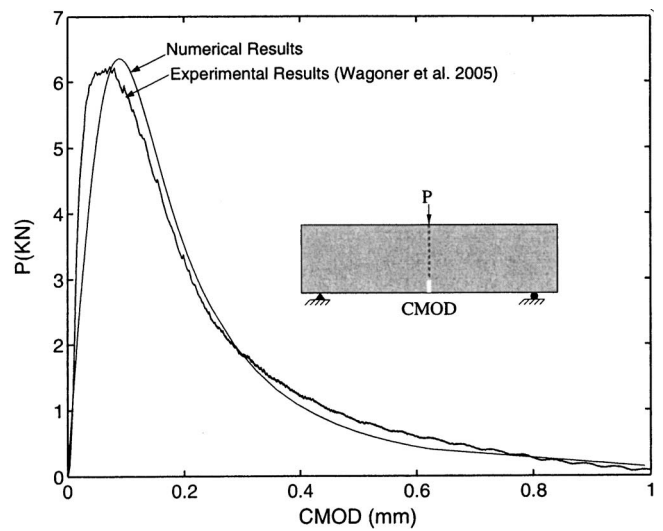


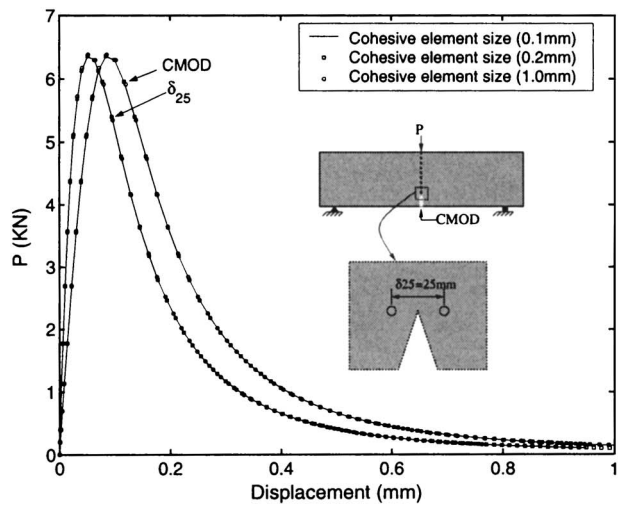
Fig. 8. Comparison between experimental result and numerical result with calibrated parameters

rule in choosing the element size is that there should be at least three elements or so along the fracture process zone. For some specific brittle materials, the fracture process zone can be estimated theoretically (Rice 1968) as

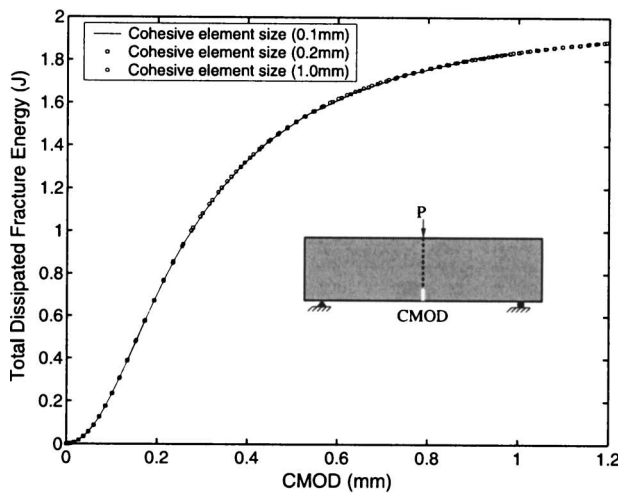
$$l_c = \frac{\pi}{8} \frac{E}{1 - \nu^2} \frac{G_c}{\sigma_{ave}^2} \quad (16)$$

where G_c = cohesive fracture energy; and σ_{ave} = measure of material strength in an average sense. However, this estimation is not valid for materials such as asphalt concrete, which is quasi-brittle and viscoelastic, because Eq. (16) is evaluated based on the assumption that energy is absorbed in a very thin cohesive zone without any consideration of viscoelastic effects. Thus, from a numerical point of view, although viscoelastic effects are not directly considered, it is crucial to make sure that the cohesive element size chosen is not sensitive to artifacts of the numerical solution.

Three different cohesive element sizes, i.e., 0.1, 0.2, and 1.0 mm, are employed. To illustrate that the cohesive element size chosen in this study is objective (i.e., somehow independent of a particular numerical solution), a local quantity, e.g., δ_{25} , and global quantities, i.e., CMOD and total dissipated energy due to fracture, are evaluated and compared. The δ_{25} , which is measured from a gauge length of 25 mm spanning the original crack tip, is introduced for operational definition of the crack tip opening displacement (CTOD) with the following advantages: It is a local quantity near the crack tip, and it can be applied to any cracked specimen due to direct and easy measurement of CTOD. The proposed δ_{25} measurement is inspired by the work by Schwalbe and Cornec (1991) and Schwalbe (1995), who proposed the insightful δ_5 concept. Notice that the original concept of δ_5 was developed and has been applied for fine-grain-sized materials like steel (Castrodeza et al. 2004). However, due to the coarse microstructure of asphalt concrete (e.g., aggregate sizes ranging from 4.75 to 19 mm in this study), a δ -type evaluation on the order of 25 mm is more appropriate, leading, for instance, to the δ_{25} definition. A numerical investigation of δ_{25} will be provided in the next example [a schematic is provided in Fig. 9(a)]. Theoretical verification and experimental validation for the proposed δ_{25} will be addressed in subsequent investigations.



(a)



(b)

Fig. 9. Comparison of: (a) P versus CMOD and δ_{25} ; (b) CMOD versus total dissipated fracture energy for different cohesive element sizes: $l_1=0.1$ mm, $l_2=0.2$ mm, and $l_3=1.0$ mm (l_i introduces a length-scale in the problem)

The geometry, boundary conditions, material properties, and nonlinear numerical scheme used here are the same as those used in the section that discussed the calibration of cohesive parameters. Thus, notice that calibrated cohesive parameters are employed. Fig. 9(a) illustrates P (applied force) versus displacement curves in which both CMOD and δ_{25} are plotted together. Fig. 9(b) shows the consumption of the cohesive fracture energy as the crack propagates. The abscissa indicates the CMOD and the ordinate indicates the total dissipated fracture energy. Due to accumulation of the cohesive fracture energy, this shows an increasing trend of the total dissipated fracture energy with an increase of the CMOD. Both the global and local responses as a function of different cohesive element sizes are nearly identical, demonstrating that the cohesive elements chosen in this particular investigation are small enough to be insensitive to numerical artifacts.

Mixed-Mode SE(B)

Using the calibrated cohesive parameters and the cohesive element size 1.0 mm, a simulation of mixed-mode crack propagation

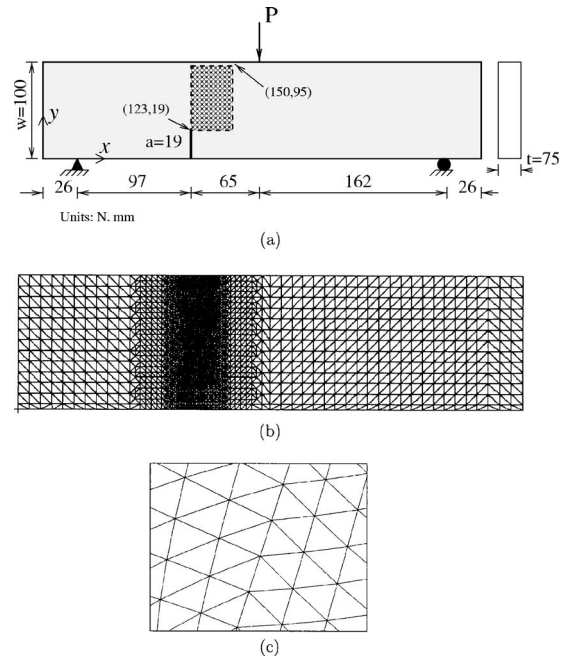
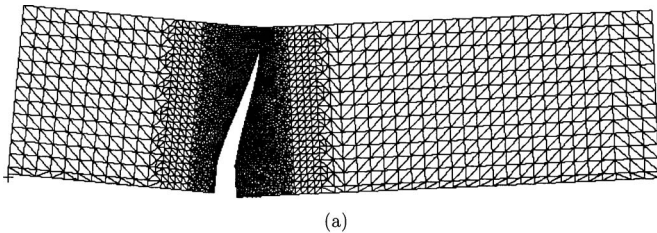


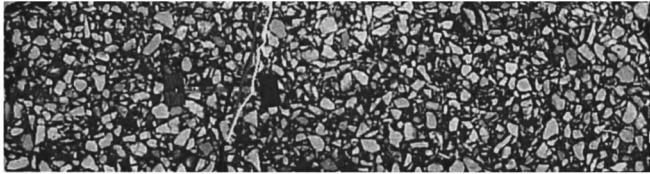
Fig. 10. Mixed-mode SE(B) test: (a) geometry and boundary condition; (b) mesh configuration for whole geometry; and (c) mesh detail where cohesive elements are inserted (dotted line indicates an area where cohesive elements are inserted)

in the SE(B) test is carried out. The cohesive elements are inserted over an area to allow cracks to propagate in any direction. Fig. 10(a) shows the geometry, boundary condition, and region enclosed by the dashed lines. The length, height, and thickness are 376, 100, and 75 mm, respectively. The crack tip is located at 65 mm to the left of and 19 mm above the center of the bottom edge. The displacement boundary condition is applied at the center of the top edge of the model. The cohesive elements are inserted over the area enclosed by the dashed lines. Fig. 10(b) illustrates finite-element discretization for the whole geometry and Fig. 10(c) shows finite-element mesh details of the region where the cohesive elements are inserted. The SE(B) structure is constructed by 5,810 three-noded triangular elements for bulk materials and by 1,010 four-noded linear elements for cohesive materials. Notice that, in order to avoid the numerical problem of nonconvergence, the mesh of Fig. 10(c) is tailored to the crack trajectory predicted by I-Franc2D (Kim 2003) and the Riks method (Crisfield 1980) is employed for this simulation.

Fig. 11(a) shows the final deformed shapes, which can be obtained with convergent solutions using the Riks method. A magnification factor of 10 is used to make the crack trajectory visible. We observed that, when the Newton-Raphson method is adopted, the cracks begin to grow, but eventually the solution diverges when a crack tip reaches around 40% of the height of the SE(B) specimen. The main reason for the nonconvergence in the CZM is that, during the quasi-static calculation, we often reach a point where the incremental solution jumps back and forth between two near equilibrium states (Tijssens et al. 2000). However, in this study, this numerical problem is not observed when the Riks method is employed, indicating its superior performance as compared to the Newton-Raphson method. Fig. 11(b) illustrates a comparison of the crack trajectory between the experimental and numerical results obtained using the Riks method. Green and blue lines indicate the crack trajectory of the front and back side of the



(a)



(b)

Fig. 11. Simulation of mixed-mode SE(B) test: (a) deformed shape showing crack trajectory (scale factor is three); (b) comparison of crack trajectory between numerical and experimental results [red line indicates crack trajectory obtained from 2D CZM; blue line and green lines denote crack trajectory from experiment (front and back faces, respectively)]

specimen based on the experimental results, respectively. The red line indicates the numerical result, which is in good agreement with the experimental results.

Summary and Conclusions

A potential-based cohesive zone model was developed and implemented using an ABAQUS user-specified element (UEL) and was subsequently employed to simulate crack propagation observed in asphalt concrete laboratory fracture tests conducted with an SE(B) apparatus. An exponential form for the free energy potential was used for the constitutive model in the cohesive elements. To verify the CZM implementation into the UEL of ABAQUS, the slender double cantilever beam is chosen and analyzed. The numerical results from this simulation matched the analytical solution remarkably well even for small crack extensions, which included boundary effects. Using the cohesive parameters obtained from the experiment, i.e., the material strength from the IDT test and the fracture energy from the SE(B), a simulation of the SE(B) fracture test was performed to calibrate cohesive parameters. Overall, the trend, peak load, and corresponding CMOD of the present numerical results with the calibrated cohesive parameters matched well with experimental results. Numerical solutions were found to be insensitive to the three cohesive element sizes investigated, e.g., 0.1, 0.2, and 1.0 mm. As the intrinsic CZM fracture energy increased, the peak load and the area under the P-CMOD curve increased as expected. Likewise, increasing the critical strength used in the intrinsic model resulted in an increase in the peak load of the simulated SE(B) experiment.

Mixed-mode crack propagation simulation of the SE(B) test was performed using the calibrated cohesive parameters. In this analysis, the cohesive elements were inserted over an area to allow crack propagation along an arbitrary direction. To avoid the numerical problem of nonconvergence, the Riks method was employed. The crack trajectory predicted by the numerical simulation was found to compare favorably to experimental results.

Acknowledgments

We are grateful for the support from the Koch Materials Company and the National Science Foundation (NSF) through the GOALI project CMS 0219566 (Program Manager, P. N. Balaguru). Any opinions expressed herein are those of the writers and do not necessarily reflect the views of the sponsors.

References

- AASHTO. (1996). "Standard test method for determining the creep compliance and strength of hot mix asphalt (HMA) using the indirect tensile test device." *AASHTO TP9-96*, Washington, D.C.
- ABAQUS user's manual, version 6.3. (2002). Hibbit, Karlsson, and Sorenson, Pawtucket, R.I.
- Abdulshafi, A. A., and Majidzadeh, K. (1985). "J-integral and cyclic plasticity approach to fatigue and fracture of asphalt mixes." *Transportation Research Record*, 1034, Transportation Research Board, Washington, D.C.
- Anderson, T. L. (1995). *Fracture mechanics: Fundamentals and applications*, CRC, Boca Raton, Fla.
- Barenblatt, G. I. (1959). "The formation of equilibrium cracks during brittle fracture: General ideas and hypothesis, axially symmetric cracks." *Appl. Math. Mech.*, 23, 622–636.
- Barenblatt, G. I. (1962). "Mathematical theory of equilibrium cracks in brittle fracture." *Adv. Appl. Math.*, 7, 55–129.
- Bhurke, A. S., Shih, E. E., and Drzal, L. T. (1997). "Fracture morphology and fracture toughness measurement of polymer-modified asphalt concrete." *Transportation Research Record*, 1590, Transportation Research Board, Washington, D.C., 23–33.
- Camacho, G. T., and Ortiz, M. (1996). "Computational modeling of impact damage in brittle materials." *Int. J. Solids Struct.*, 33, 2899–2938.
- Castell, M. A., Ingrassia, A. R., and Irwin, L. H. (2000). "Fatigue crack growth in pavements." *J. Transp. Eng.*, 126(4), 283–290.
- Castrodeza, E. M., Ipinia, J. E. P., and Bastian, F. L. (2004). "Fracture toughness evaluation of unidirectional fibre metal laminates using traditional CTOD (δ) and Schwalbe (δ_s) methodologies." *Eng. Fract. Mech.*, 71, 1107–1118.
- Crisfield, M. A. (1980). "A fast incremental/iterative solution procedure that handles 'snap-through'." *Comput. Struct.*, 13, 55–62.
- Dugdale, D. (1960). "Yielding of steel sheets containing slits." *J. Mech. Phys. Solids*, 8, 100–104.
- Espinosa, H. D., and Zavattieri, P. D. (2003). "A grain level model for the study of failure initiation and evolution in polycrystalline brittle materials. Part I: Theory and numerical implementation." *Mech. Mater.*, 35, 333–364.
- Jacobs, M. M., Hopman, P. C., and Molenaar, A. A. A. (1996). "Application of fracture mechanics in principles to analyze cracking in asphalt concrete." *Proc., Association of Asphalt Paving Technologists*, Association of Asphalt Paving Technologists, White Bear Lake, Minn., 65, 1–39.
- Jin, Z.-H., Paulino, G. H., and Dodds, R. H., Jr. (2003). "Cohesive fracture modeling of elastic-plastic crack growth in functionally graded materials." *Eng. Fract. Mech.*, 70, 1885–1912.
- Kim, J.-H. (2003). "Mixed-mode crack propagation in functionally graded materials." Ph.D. thesis, Dept. of Civil and Environmental Engineering, Univ. of Illinois at Urbana-Champaign, Urbana, Ill.
- Kim, K. W., and El Hussein, H. M. (1995). "Effect of differential thermal contraction on fracture properties of asphalt materials at low temperature." *Proc., Association of Asphalt Paving Technologists*, Association of Asphalt Paving Technologists, White Bear Lake, Minn., 64, 474–499.
- Klein, P. A., Foulk, J. W., Chen, E. P., Wimmer, S. A., and Gao, H. (2001). "Physics-based modeling of brittle fracture: Cohesive formu-

- lations and the applications of meshfree methods." *SAND 2001-8009*, Sandia National Laboratories, Albuquerque, N.M.
- Majidzadeh, K., Kauffmann, E. M., and Ramsamooj, D. V. (1971). "Application of fracture mechanics in the analysis of pavement fatigue." *Proc., Association of Asphalt Paving Technologists*, Association of Asphalt Paving Technologists, White Bear Lake, Minn., 40, 227–246.
- Mosalam, K. M., and Paulino, G. H. (1997). "Evolutionary characteristics length method for smeared cracking finite element models." *Finite Elem. Anal. Design*, 27, 99–108.
- Ortiz, M., and Pandolfi, A. (1999). "Finite deformation irreversible cohesive elements for the three dimensional crack propagation analysis." *Int. J. Numer. Methods Eng.*, 44, 1267–1282.
- Owusu-Antwi, E. B., Khazanovich, L., and Titus-Glover, L. (1998). "A mechanistic-based model for predicting reflective cracking in AC overlaid pavements." *Proc., Annual Meeting*, Transportation Research Board, Washington, D.C.
- Paulino, G. H., Jin, Z. H., and Dodds, R. H., Jr. (2003). "Failure of functionally graded materials." *Comprehensive structural integrity*, Vol. 2, B. Karihaloo and W. G. Knauss, eds., Elsevier, New York, 607–644.
- Paulino, G. H., Song, S. H., and Buttlar, W. G. (2004). "Cohesive zone modeling of fracture in asphalt concrete." *Proc., 5th RILEM Int. Conf. on Cracking in Pavements: Mitigation, Risk Assessment and Prevention*, C. Petite, I. Al-Qadi, and A. Millien, eds., RILEM, Cachan Cedex, France, 63–70.
- Rahulkumar, P., Jagota, A., Bennison, S. J., and Saigal, S. (2000). "Cohesive element modeling of viscoelastic fracture: Application to peel testing of polymers." *Int. J. Solids Struct.*, 37, 1873–1897.
- Rice, J. R. (1968). "Mathematical analysis in the mechanics of fracture." *Fracture: An advanced treatise*, H. Liebowitz, ed., Academic, New York, 191–311.
- Roy, Y. A., and Dodds, R. H., Jr. (2001). "Simulation of ductile crack growth in thin aluminum panels using 3-D surface cohesive elements." *Int. J. Fract.*, 110, 21–45.
- Ruiz, G., Pandolfi, A., and Ortiz, M. (2001). "Three-dimensional cohesive modeling of dynamic mixed-mode fracture." *Int. J. Numer. Methods Eng.*, 52, 97–120.
- Sangpetngam, B., Birgisson, B., and Roque, R. (2004). "A multi-layer boundary element method for the evaluation of top-down cracking in hot mix asphalt pavements." *Proc., Annual Meeting* (CD-ROM), Transportation Research Board, Washington, D.C.
- Schwalbe, K.-H. (1995). "Introduction of δ_5 as an operational definition of the CTOD and its practical use." *Fracture mechanics*, Vol. 26, ASTM, West Conshohocken, Pa., 763–778.
- Schwalbe, K.-H., and Cornec, A. (1991). "The engineering treatment model (ETM) and its practical application." *Fatigue Fract. Eng. Mater. Struct.*, 14(4), 405–412.
- Shen, W., and Kirkner, D. J. (1999). "Distributed thermal cracking of AC pavement with frictional constraint." *J. Eng. Mech.*, 125(5), 554–560.
- Siegmund, T., and Needleman, A. (1997). "A numerical simulation of fast crack growth in brittle solids." *J. Mech. Phys. Solids*, 42, 1397–1434.
- Soares, J. B., Colares de Freitas, F. A., and Allen, D. H. (2003). "Crack modeling of asphaltic mixtures considering heterogeneity of the material." *Proc., Annual Meeting*, Transportation Research Board, Washington, D.C.
- Song, S. H., Paulino, G. H., and Buttlar, W. G. (2005). "Simulation of mode I and mixed-mode crack propagation in asphalt concrete using a bilinear cohesive zone model." *Proc., Annual Meeting* (CD-ROM), Transportation Research Board, Washington, D.C.
- Tijssens, M. G. A., Sluys, B. L. J., and Giessen, E. V. D. (2000). "Numerical simulation of quasi-brittle fracture using damaging cohesive surfaces." *Eur. J. Mech. A/Solids*, 19, 761–779.
- Tvergaard, V. (1990). "Effect of fiber debonding in a whisker-reinforced metal." *Mater. Sci. Eng.*, 125, 203–213.
- Tvergaard, V., and Hutchinson, J. W. (1992). "The relation between crack growth resistance and fracture process parameters in elastic-plastic solids." *J. Mech. Phys. Solids*, 40(6), 1377–1397.
- Wagoner, M.P., Buttlar, W. G., and Paulino, G. H. (2005). "Development of a single-edge notched beam test for asphalt concrete mixtures." *J. Test. Eval.*, 33(6), 452–460.
- Xu, X.-P., and Needleman, A. (1994). "Numerical simulations of fast crack growth in brittle solids." *J. Mech. Phys. Solids*, 42(9), 1397–1434.